

Magnetospheric flux transport in the Dungey cycle during 2010

Stephen E. Milan¹, Jennifer Alyson Carter¹, Harneet Sangha¹, Gemma E. Bower¹, and Brian J. Anderson²

¹University of Leicester

²John Hopkins Univ.

November 22, 2022

Abstract

We quantify the contributions of different convection states to the magnetic flux throughput of the magnetosphere during 2010. To do this we provide a continuous classification of convection state for the duration of 2010 based upon observations of the solar wind and interplanetary magnetic field, geomagnetic indices, and field-aligned currents measured by the Active Magnetosphere and Planetary Electrodynamics Response Experiment (AMPERE). Convection states are defined as 1) quiet and 2) weak activity, substorm 3) growth, 4) expansion, and 5) recovery phases, 6) substorm driven phase (when relatively steady magnetospheric convection occurs), 7) recovery bays (when recovery phase is accompanied by a negative excursion of the AL electrojet index), and 8) periods of multiple intensifications (storm-time periods when continuous short-period AL activity occur). The magnetosphere is quiet for 46% of the time, when very little convection takes place. The majority of convection occurs during growth and driven phases (21% and 38%, respectively, of open magnetic flux accumulation by dayside reconnection). We discuss these results in the context of the expanding/contracting polar cap model of convection, and describe a framework within which isolated substorms and disturbances during periods of more continuous solar wind-magnetosphere driving can be understood.

Abstract

We quantify the contributions of different convection states to the magnetic flux throughput of the magnetosphere during 2010. To do this we provide a continuous classification of convection state for the duration of 2010 based upon observations of the solar wind and interplanetary magnetic field, geomagnetic indices, and field-aligned currents measured by the Active Magnetosphere and Planetary Electrodynamics Response Experiment (AMPERE). Convection states are defined as 1) quiet and 2) weak activity, substorm 3) growth, 4) expansion, and 5) recovery phases, 6) substorm driven phase (when relatively steady magnetospheric convection occurs), 7) recovery bays (when recovery phase is accompanied by a negative excursion of the AL electrojet index), and 8) periods of multiple intensifications (storm-time periods when continuous short-period AL activity occur). The magnetosphere is quiet for 46% of the time, when very little convection takes place. The majority of convection occurs during growth and driven phases (21% and 38%, respectively, of open magnetic flux accumulation by dayside reconnection). We discuss these results in the context of the expanding/contracting polar cap model of convection, and describe a framework within which isolated substorms and disturbances during periods of more continuous solar wind-magnetosphere driving can be understood.

Plain Language Summary

Space weather within the Earth’s geospace environment, including vivid auroral displays and geomagnetic activity that is damaging for satellites, telecommunications, global positioning systems, power distribution and pipelines, is caused by the interaction between the solar wind and the terrestrial magnetic field. We use observations of the solar wind, electric currents in the magnetosphere, and magnetic perturbations on the ground to analyse geomagnetic activity continuously for the whole of 2010. This allows us to determine that a range of responses are excited in the magnetosphere by different solar wind conditions, and to quantify the solar wind conditions that lead to most activity.

1 Introduction

In this study we provide a continuous classification of magnetospheric convection state for the duration of 2010 to quantify the overall contributions of different states to the magnetic flux throughput of the system. Such activity is driven by magnetic reconnection at the dayside magnetopause, interlinking the Earth’s magnetic field with the interplanetary magnetic field (IMF) carried by the solar wind, and the subsequent release of the IMF by reconnection in the magnetotail, together exciting the Dungey cycle of convection (Dungey, 1961). Variability of the dayside reconnection rate leads to a variety of time-dependent responses of the magnetosphere, most notably substorms and periods of steady magnetospheric convection, which can be described by the expanding/contracting polar cap model or ECPC (Cowley & Lockwood, 1992; Lockwood & Cowley, 1992; Milan, 2015). The ECPC has been employed to investigate the response of the magnetosphere to solar wind driving, either as case studies of a limited number of events (e.g., Milan et al., 2003, 2007, 2008; Milan, 2004; Hubert et al., 2006, 2017), or as statistics of many events (e.g., Milan, Grocott, et al., 2009; Milan, Hutchinson, et al., 2009; Clausen et al., 2013; Coxon et al., 2014; Walach & Milan, 2015; Milan et al., 2019). A drawback of such studies has been that they tend to focus on “interesting” periods rather a longitudinal analysis of geomagnetic activity (or lack thereof) over a prolonged period of time. To our knowledge, only Lockwood et al. (2009) have previously attempted a continuous breakdown of activity over an extended interval (the duration of 2001).

Previous workers have compiled lists of substorm onsets (e.g., Frey et al., 2004; Newell & Gjerloev, 2011; Forsyth et al., 2015) or periods of steady magnetospheric convection (e.g., Kissinger et al., 2011) using, for instance, magnetometer measurements (usually

64 the AU/AL electrojet indices) or global auroral imagery. These provide a useful frame-
 65 work for interpreting other geophysical observations. However, they tend to be based on
 66 a single observable that can be misinterpreted in isolation (e.g., Walach & Milan, 2015).
 67 In addition, “onset lists” do not provide information on the magnetospheric behaviour
 68 between onsets. In this study we employ a variety of solar wind and magnetospheric in-
 69 dicators with the aim of (a) reducing ambiguity in the determination of convection state
 70 and (b) providing an unbroken record of convection state over a prolonged period of time.

71 The rate of change of open (polar cap) flux, F_{PC} , is determined by the competi-
 72 tion between the dayside (magnetopause) reconnection rate, Φ_D , and the nightside (mag-
 73 netotail) reconnection rate, Φ_N ,

$$\frac{dF_{PC}}{dt} = \Phi_D - \Phi_N, \quad (1)$$

74 (Siscoe & Huang, 1985; Cowley & Lockwood, 1992; Milan et al., 2015). Φ_D is the rate
 75 at which magnetospheric flux is opened, usually assumed to occur at the low latitude
 76 magnetopause; it does not include high latitude lobe reconnection as this produces no
 77 net opening of flux. Reconnection in the magnetotail can occur either at a distant neu-
 78 tral line (DNL) or near-Earth neutral line (NENL) (Hones Jr., 1984; Baker et al., 1996).
 79 Φ_N refers specifically to the reconnection site that is actively closing open lobe flux; al-
 80 though in principle both a DNL and NENL can be active simultaneously, only one con-
 81 tributes to Φ_N . Consider a situation in which a NENL forms during a period when a pre-
 82 existing DNL is active and closing flux at a rate Φ_N . Initially the NENL will reconnect
 83 closed flux to grow a plasmoid, but will not contribute to Φ_N . If the NENL recon-
 84 nection rate exceeds the DNL rate, then eventually the plasmoid will be pinched off, at which
 85 point the NENL will dictate Φ_N , the DNL now sitting on disconnected field lines prop-
 86 agating down-tail with the plasmoid (see also discussion in Russell (2000)).

87 As F_{PC} increases or decreases with time, and the magnetotail correspondingly in-
 88 flates or deflates, flows are excited in the magnetosphere and ionosphere to maintain the
 89 magnetopause in stress balance with the flow of the solar wind (Cowley & Lockwood,
 90 1992). Convection is quantified as the rate of transport of magnetic flux by these flows
 91 through the magnetosphere and across the polar cap, known as the cross-polar cap po-
 92 tential or transpolar voltage, Φ_{PC} . Assuming that the polar cap remains roughly cir-
 93 cular as it expands and contracts,

$$\Phi_{PC} = (\Phi_D + \Phi_N)/2 \quad (2)$$

94 (Lockwood, 1991). F_{PC} is observed to remain within the range 0.2 to 1.2 GWb (Milan
 95 et al., 2007), implying that on timescales of several hours the average dayside and night-
 96 side reconnection rates must equal, such that

$$\langle \Phi_{PC} \rangle = \langle \Phi_D \rangle = \langle \Phi_N \rangle. \quad (3)$$

97 Convective flows are a major source of geomagnetic activity. Convection is asso-
 98 ciated with horizontal currents in the ionosphere, and convection shears produce field-
 99 aligned currents (FACs) that close the circuit between the ionosphere and magnetosphere.
 100 The dominant FACs are the region 1 and 2 (R1/R2) currents first described by Iijima
 101 and Potemra (1976, 1978), which are coincident with the convection reversal boundary
 102 and the equatorward boundary of the convection pattern, respectively. The locations of
 103 these FACs depend on the size of the polar cap, and hence can be used to estimate F_{PC} .
 104 Particle precipitation carrying FACs produces the main auroral oval and increases the
 105 ionospheric conductance, in turn modifying the horizontal currents. Convection and con-
 106 ductance variability, especially associated with substorms, produces the magnetic per-
 107 turbations measured as geomagnetic activity by the upper and lower auroral electrojet
 108 indices, AU and AL (Davis & Sugiura, 1966). Convection also controls the injection of
 109 plasma into the inner magnetosphere and its energisation, leading to enhancements of

110 the ring current and storm-time magnetic perturbations measured by the SYM-H index
111 (Iyemori, 1990).

112 The behaviour of the magnetosphere depends largely on the interplay between Φ_D
113 and Φ_N . The dayside reconnection rate is directly and promptly controlled by conditions
114 in the solar wind, including its speed and the magnitude and orientation of the embed-
115 ded interplanetary magnetic field (IMF) (Milan et al., 2012, and references therein). The
116 nightside reconnection rate is somewhat decoupled from the dayside rate, though must
117 balance the dayside rate over periods of several hours, is described by eq. (3). As F_{PC}
118 increases the magnetotail becomes inflated and the magnetopause flares outwards, in-
119 tercepting the flow of the solar wind. The pressure exerted by the solar wind on the mag-
120 netopause is exerted through the magnetotail lobes and onto the plasma sheet, which
121 thins, leading to conditions conducive to the onset of magnetotail reconnection (Slavin
122 et al., 2002; Milan et al., 2006, 2008). It has also been speculated that the magnetic per-
123 turbation produced by an enhanced ring current can counteract this thinning and inhibit
124 the onset of reconnection (Milan, Hutchinson, et al., 2009). Then, the onset of tail re-
125 connection is a competition between these two influences.

126 The behaviour is usually described in terms of the growth, expansion, and recov-
127 ery phases of the substorm cycle (McPherron, 1970; McPherron et al., 1973; Rostoker
128 et al., 1980; Lockwood & Cowley, 1992). The growth phase follows a southward turn-
129 ing of the IMF, $\Phi_D > 0$ and $\Phi_N \approx 0$ such that $dF_{PC}/dt > 0$, the polar cap expands
130 and the auroral oval progresses to lower latitudes. At some point reconnection is initi-
131 ated in the magnetotail (see above), $\Phi_N > 0$, and intense auroras form the substorm
132 auroral bulge, which tends to expand polewards as open flux is closed, known as the sub-
133 storm expansion phase. The auroral bulge is associated with the formation of the sub-
134 storm current wedge and westward substorm electrojet which produces a sharp negative
135 excursion in the AL index – the substorm bay. A northward turning of the IMF then
136 leads to substorm recovery phase, during which $\Phi_D \approx 0$ but persistent magnetotail re-
137 connection, $\Phi_N > 0$, leads to $dF_{PC}/dt < 0$, the polar cap contracts and the auroral
138 oval progresses to higher latitudes. Eventually nightside reconnection switches off and
139 the magnetosphere enters a quiescent state. Between the expansion and recovery phases,
140 if the IMF remains southwards for a prolonged period, the nightside reconnection rate
141 can settle such that $\Phi_N \approx \Phi_D$ and $dF_{PC}/dt \approx 0$ (Walach & Milan, 2015; Milan et
142 al., 2019). Periods of $\Phi_N \approx \Phi_D$ have been known as balanced reconnection intervals
143 (BRIs) (DeJong et al., 2008), periods of steady magnetospheric convection (SMC) (Sergeev
144 et al., 1996; McWilliams et al., 2008; Kissinger et al., 2012), convection bays (Sergeev
145 et al., 2001), and steady convection events (SCE) (Lockwood et al., 2009). We now in-
146 troduce the term driven phase to describe this aspect of the substorm cycle.

147 In Section 2 we describe the observables we use in this study and the convection
148 states that we identify. Section 3 presents an analysis of the occurrence of different states
149 and the sequences of states that represent substorms and other forms of geomagnetic ac-
150 tivity. Finally, we conclude and describe future directions for research in Section 4.

151 2 Methodology

152 We determine magnetospheric convection state continuously for the duration of 2010.
153 A few data gaps are present in the data, and the total period of analysis comprises just
154 over 360 full days. Figure 1 shows a 60 h interval from May, which we discuss below. This
155 interval is chosen as it is typical, but also contains examples of all the convection states
156 discussed in this paper.

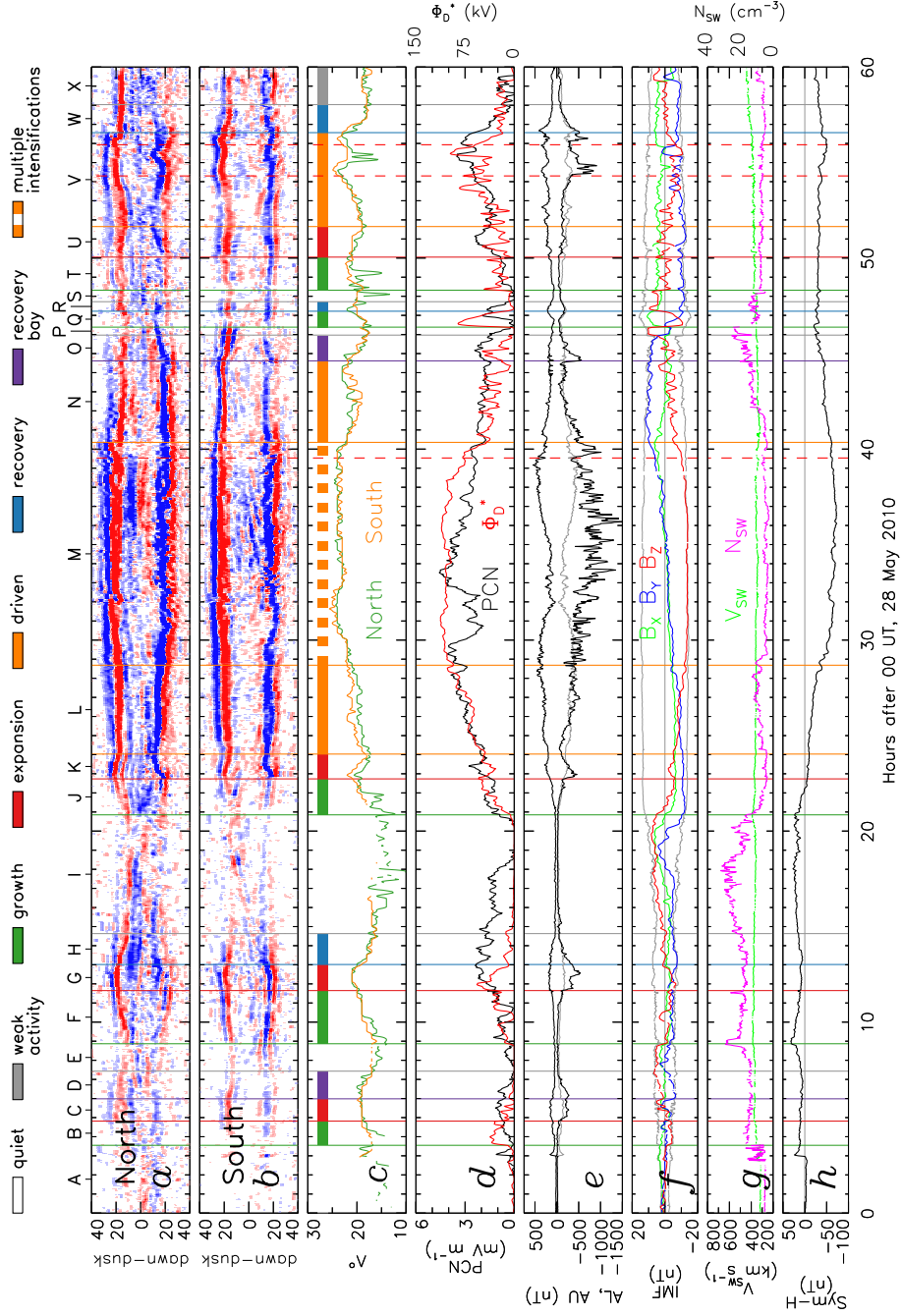


Figure 1. Observations and magnetospheric state classifications for a 60 h period following 00 UT, 28 May 2010. (a) and (b) Keograms of AMPERE field-aligned currents across the dawn-dusk meridian in the Northern and Southern Hemispheres. Red and blue represent upward and downward FACs, the colour scale saturating at $\pm 0.5 \mu\text{A m}^{-2}$. (c) The radius of a circle fitted to the boundary between R1 and R2 currents, Λ , in the two hemispheres, which is a proxy for polar cap flux F_{PC} . (d) The PCN geomagnetic index, a proxy for cross-polar cap potential Φ_{PC} , and Φ_D^* , a proxy for dayside reconnection rate. (e) AU and AL (black lines); -AU (grey line) for comparison with AL. (f) The B_X , B_Y , and B_Z components of the IMF. (g) Solar wind speed, V_{SW} , and density, N_{SW} . (h) The SYM-H geomagnetic index.

157

2.1 Parameters

158

159

160

161

162

163

Our classification of convection state is based on a consideration of the auroral electrojet indices, AU and AL, dayside and nightside reconnection rates, polar cap open flux and the cross-polar cap potential. F_{PC} , Φ_D , Φ_N , and Φ_{PC} are important parameters for understanding magnetospheric convection, though in general are difficult to measure accurately. As described below we use proxies, F_{PC}^* , Φ_D^* , and Φ_{PC}^* , for three of these parameters; Φ_N can be inferred from these using eqs. (1) and (2).

164

165

166

167

168

169

170

171

172

Additional parameters are included in the analysis, but are not used to determine the state classifications: the geomagnetic index SYM-H, the solar wind speed and density, and IMF magnitude and orientation. Geomagnetic indices and solar wind parameters are derived from the 1-min OMNI dataset (King & Papitashvili, 2005). We also use observations of FACs from the Advanced Magnetosphere and Planetary Electrodynamics Response Experiment (AMPERE) which uses magnetometer measurements from the Iridium telecommunications constellation to infer currents poleward of 40° geomagnetic latitude at a cadence of 2 min (see e.g., Anderson et al., 2000, 2002; Waters et al., 2001; Coxon et al., 2018).

173

2.1.1 FAC radius, Λ , and polar cap flux, F_{PC}^*

174

175

176

177

178

179

Monitoring the polar cap or open magnetic flux is important for interpreting magnetospheric dynamics in the context of the ECPC model. Previous studies that have used global auroral imagery to estimate F_{PC} have faced the limitation that gaps in observation occur every orbit (e.g., Milan et al., 2007; Milan, Hutchinson, et al., 2009; Milan, 2009). AMPERE, on the other hand, provides continuous observations of the FACs in both hemispheres, with few breaks in continuity.

180

181

182

183

184

185

186

187

188

189

190

191

Panels (a) and (b) of Fig. 1 show keograms of AMPERE FACs along the dawn-dusk meridian of the Northern and Southern Hemispheres. The up/down pairs of R1 and R2 currents can be seen at both dawn and dusk, varying in magnitude with the strength of convection and moving in colatitude as the polar cap expands and contracts (Clausen et al., 2012; Milan, 2013; Milan et al., 2017, 2019). We use the radius of a circle fitted to the boundary between R1 and R2 FACs, determined using the method of Milan et al. (2015), as a proxy for F_{PC} . Fig. 1(c) shows this radius, Λ , determined independently from the FACs in both hemispheres. Λ can only be measured when the FACs are of sufficient magnitude that the boundary between R1 and R2 is readily identifiable. This occurs frequently in the summer hemisphere where the ionospheric conductance is high, and in the winter hemisphere when convection is active. The measurements from the two hemispheres are combined to provide a single estimate of Λ .

192

193

194

195

196

197

198

199

200

Burrell et al. (2020) confirmed that Λ is related to the location of the OCB, using DMSP spacecraft particle measurements. Figure 2(a) shows the relationship between Λ and our proxy F_{PC}^* , assuming that the polar cap boundary lies $\Delta\Lambda = 3^\circ$ or 4° poleward of the R1/R2 boundary. F_{PC}^* is calculated as the radial component of a dipole field integrated over the polar regions within a circle of radius $\Lambda - \Delta\Lambda$, centred on a point displaced from the geomagnetic pole by 4° along the midnight meridian, the typical centre of the auroral oval and the R1/R2 FAC rings (this curve is insensitive to the choice of pole offset in the range 0° to 10°). Assuming $\Delta\Lambda = 4^\circ$, a convenient relation between Λ° and F_{PC}^* (GWb) over the range shown is

$$F_{PC}^* \approx 0.00182 \Lambda^2 - 0.009 \Lambda - 0.02, \quad (4)$$

201

202

203

204

205

indicated by the red line in Fig. 2(a). Figs. 2(b) and (c) show the occurrence and cumulative occurrence distributions of Λ in 2010; the median value is close to 17.5° , corresponding to $F_{PC}^* \approx 0.4$ GWb, which is close to previous estimates of the typical polar cap size, made using different observational techniques (e.g., Milan et al., 2007; Boakes et al., 2008).

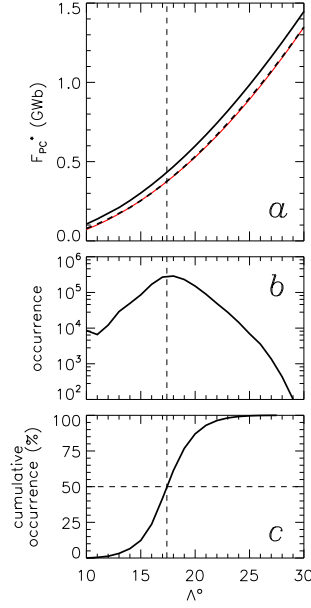


Figure 2. (a) Relationship between Λ and F_{PC}^* assuming that the polar cap boundary is circular and located 3° (full line) or 4° (dashed line) poleward of the boundary between R1 and R2 FACs. The red line shows eq. (4). (b) The occurrence distribution of Λ measured during 2010. (c) The associated cumulative occurrence distribution, showing that the median $\Lambda \approx 17.5^\circ$, or the median $F_{PC}^* \approx 0.4$ GWb.

206 As will be discussed below, F_{PC}^* overestimates the true value of F_{PC} when a sig-
 207 nificant auroral bulge is present, as the assumption of the circularity of the polar cap breaks
 208 down (Mooney et al., 2020).

209 **2.1.2 Dayside reconnection rate, Φ_D^***

210 The low latitude magnetopause reconnection rate is predicted from the upstream
 211 solar wind speed and (GSM) interplanetary magnetic field components using the param-
 212 eterisation of Milan et al. (2012):

$$\Phi_D^* = 3.2 \times 10^5 V_{SW}^{4/3} B_{YZ} \sin^{9/2} \left| \frac{\theta}{2} \right|, \quad (5)$$

213 where $\theta = \tan^{-1}(B_Y, B_Z)$ is the IMF clock angle and $B_{YZ}^2 = B_Y^2 + B_Z^2$.

214 Figure 3 tests the relationship between Φ_D^* and F_{PC}^* expected from eq. (1), using
 215 data from 23 October 2010. Panel (a) shows Λ determined from AMPERE at 2 min ca-
 216 dence (grey curve), and with a Savitsky-Golay filter (11 point window, degree 3 poly-
 217 nomial) applied to provide smoothing (black curve). Repeated increases and decreases
 218 in Λ indicate substorm cycles (Milan et al., 2007; Clausen et al., 2012). In panel (d) Λ
 219 has been converted to F_{PC}^* using eq. (4). Panel (c) shows Φ_D^* evaluated at 2 min cadence.
 220 Multiple data gaps in V_{SW} create gaps in Φ_D^* , and where these are less than 10 min in
 221 duration we have linearly interpolated over the missing values.

222 Superimposed on panel (d) are curves of $\int \Phi_D^* dt$ (red dashes), which predict from
 223 eq. (1) how F_{PC} should grow with time, assuming that $\Phi_N = 0$. Each of these curves
 224 is the same, but each has been vertically offset to match the variation in F_{PC}^* , blue cir-
 225 cles indicating the points at which the matching has been performed. Vertical green and
 226 red lines indicate the starts of growth and expansion phases identified in the data (see

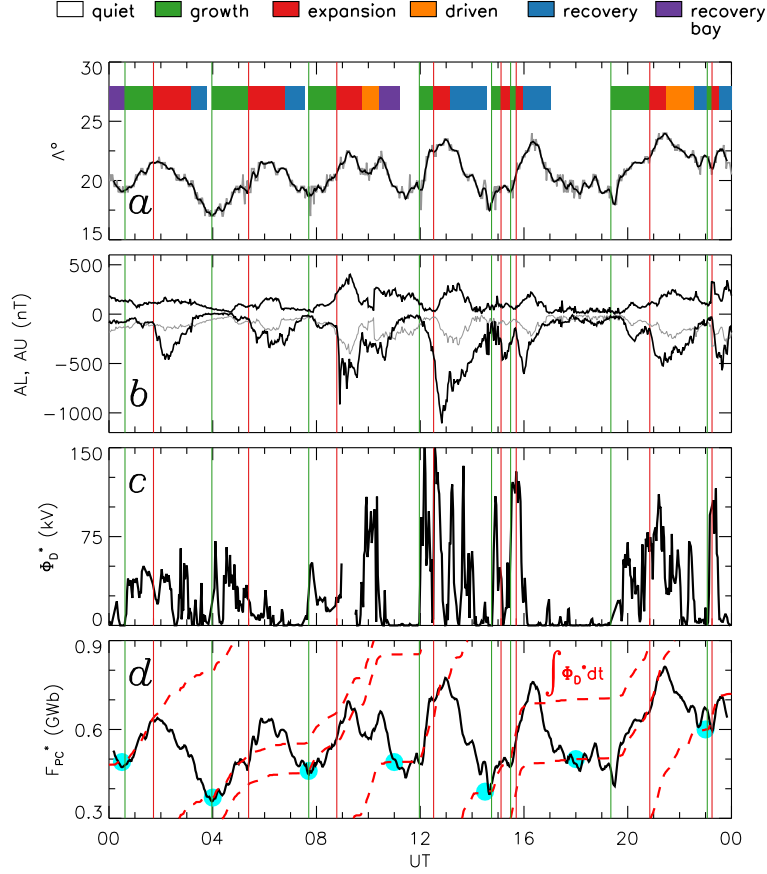


Figure 3. A comparison of polar cap size and dayside reconnection rate from 23 October 2010. (a) Radius of the R1/R2 field-aligned current boundary, Λ , measured by AMPERE (grey) and smoothed with a Savitsky-Golay filter (black). Convection state is indicated by coloured bars; green and red vertical lines indicate the start of growth and expansion phases. (b) AU and AL electrojet indices. (c) Dayside reconnection rate estimated from OMNI solar wind observations, Φ_D^* . (d) Polar cap flux estimated from Λ , F_{PC}^* . Superimposed are multiple copies of the curve $\int \Phi_D^* dt$, vertically offset to align with F_{PC}^* during growth phases; blue circles indicate where the curves have been matched up.

below); AU and AL are presented in panel (b) for reference. It is found that the growth in F_{PC}^* and $\int \Phi_D^* dt$ match reasonably well during growth phases, giving confidence in our use of these proxies.

The vertical offset between subsequent $\int \Phi_D^* dt$ curves indicates the amount of flux that has been closed in the intervening activity of each substorm, that is $\int \Phi_N dt$. In principle, Φ_N can be estimated from these observations (Hubert et al., 2006; Milan et al., 2007), but we have not done this in the present study.

2.1.3 Polar cap index, PCN, and cross-polar cap potential, Φ_{PC}^*

The polar cap index PCN measures the magnetic perturbation produced on the ground in the central (northern) polar cap produced by horizontal ionospheric currents associated with convection overhead (Troshichev et al., 2006). The index is scaled to closely match the magnitude of the solar wind geoeffective interplanetary electric field E_{KL} (the Kan-Lee coupling function (Kan & Lee, 1979)) and so is measured in units of mV m^{-1} . PCN is usually interpreted as solar wind energy input into the magnetosphere (Troshichev et al., 1979). However, the ionospheric flow to which the index is sensitive is the anti-sunward convection of the Dungey cycle, excited by the combined contributions of day-side and nightside reconnection, and as a consequence we use PCN as a proxy for the cross-polar cap potential, Φ_{PC} .

The transport of magnetic flux within the magnetosphere leads to ionospheric convection during growth, expansion, driven, and recovery phases. From eq. 2 we expect the cross-polar cap potential during each substorm phase to be: growth, $\Phi_{PC} \approx \Phi_D/2$; expansion, $\Phi_{PC} \approx (\Phi_D + \Phi_N)/2$; driven, $\Phi_{PC} \approx \Phi_D \approx \Phi_N$; recovery, $\Phi_{PC} \approx \Phi_N/2$. During quiescent periods we expect $\Phi_{PC} \approx \Phi_D \approx \Phi_N \approx 0$. Hence, we expect that during the typical growth-expansion-recovery phase sequence of a substorm Φ_{PC} will be a smoothed version of Φ_D , with a time lag of the order of the duration of the growth and recovery phases (Milan, 2004). A lagged cross-correlation between Φ_D^* (kV) and PCN (mV m^{-1}) indicates that $\text{PCN} \approx \Phi_D^*/17$, with a maximum correlation at a lag of approximately 30 mins (this can be confirmed by comparing variations in PCN and Φ_D^* in Fig. 1(d)). Our proxy for the cross-polar cap potential is then Φ_{PC}^* (kV) ≈ 17 PCN.

We note that during strong northward IMF conditions PCN can respond to polar cap flows driven by lobe reconnection, rather than being associated with the antisunward flow of the Dungey cycle, and is then not a good proxy for Φ_{PC} .

2.1.4 Electrojet indices, AU and AL

AU and AL represent the maximum positive and negative northward magnetic perturbations measured at ground magnetometers located at auroral latitudes (Davis & Sugiura, 1966). During non-substorm periods these represent the strength of the eastward and westward auroral electrojets, related to the strength of convection in the Dungey cycle return flow regions, and it is expected that $|\text{AL}| \approx \text{AU}$. During substorm expansion phase the presence of the westward substorm electrojet introduces a negative perturbation to the AL index, in which case $|\text{AL}| > \text{AU}$; such a “negative bay” in AL is commonly used as an indicator of substorm onset (e.g., Newell & Gjerloev, 2011; Forsyth et al., 2015). These two aspects, convection and substorm contributions to AU and AL, have been described as the “two component auroral electrojets” by Kamide and Kokubun (1996).

2.1.5 Ring current index, SYM-H

SYM-H is the north-south magnetic perturbation produced by the westward ring current measured at low latitude ground magnetometers (Iyemori, 1990). It is also affected by the magnetopause current, which produces a positive perturbation in SYM-

274 H when the solar wind ram pressure is high. It has been suggested that the magnetic
 275 perturbation produced by the ring current in the magnetotail can modulate the occur-
 276 rence of tail reconnection (Milan, Hutchinson, et al., 2009).

277 **2.2 Magnetospheric convection state categories**

278 We subdivide 2010 into the following convection states: quiet, weak activity, sub-
 279 storm growth, expansion, driven, and recovery phases, recovery bays, and multiple in-
 280 tensifications; this dataset is available as Milan (2020). This categorisation is in the same
 281 spirit as that of Lockwood et al. (2009), though as our observations are available at higher
 282 temporal cadence, and many of our observables are different, we have adapted our def-
 283 initions and added some additional states. These classifications are shown in Fig. 1(c)
 284 and by vertical lines in other panels; intervals have been labelled A to X to aid discus-
 285 sion. In the following sections we explain how we identified these states. We note that
 286 Lockwood et al. (2009) lamented that there was no “agreed standard set of definitions
 287 [of states] which would allow comparison with other studies,” and unfortunately this is
 288 still the case.

289 **2.2.1 Quiescent**

290 Periods of low dayside reconnection and no appreciable nightside activity, $\Phi_D^* <$
 291 5 kV, $\Phi_N \approx \Phi_{PC}^* \approx 0$ are designated as *quiet* (A, E, I, P, S). Typically, the FAC cur-
 292 rents are so weak that the R1/R2 pattern is unclear and Λ cannot be determined. Dur-
 293 ing periods of strongly northward IMF, PCN may be elevated due to the occurrence of
 294 lobe reconnection, and is then not a good proxy for Φ_{PC}^* (as seen during interval I).

295 **2.2.2 Growth phase**

296 *Growth phases* (B, F, Q, and T) begin with a southward turning of the IMF, or
 297 an increase of dayside coupling to $\Phi_D^* > 10$ kV, leading to a progressive increase in Λ .
 298 AU and AL may become elevated, though $|\text{AL}| \approx \text{AU}$, indicating that there is no sig-
 299 nificant nightside activity, $\Phi_N \approx 0$. PCN can increase due to the driving of convection
 300 by dayside reconnection.

301 **2.2.3 Expansion phase**

302 Onset of the *expansion phase* (C, G, U) is typically marked by a negative excur-
 303 sion of AL (a *substorm bay*) such that $|\text{AL}| > \text{AU}$. In many cases Λ continues to increase
 304 for approximately 20 mins following expansion phase onset, but then levels off or decreases
 305 slightly indicating the onset of magnetotail reconnection with $\Phi_N \approx \Phi_D$.

306 **2.2.4 Recovery phase**

307 The start of the *recovery phase* (H, R) is marked by a northward turning of the IMF
 308 or a decrease in dayside driving to $\Phi_D^* < 5$ kV. Λ usually decreases markedly during
 309 the recovery phase due to ongoing nightside reconnection, $\Phi_N > \Phi_D$. AU, AL, and PCN
 310 tend to decrease over the course of a recovery phase. The end of the recovery phase is
 311 usually a gradual transition to quiet conditions.

312 **2.2.5 Driven phase**

313 Often, the magnetosphere does not transition directly from expansion to recovery
 314 phase, but enters a period when dayside and nightside reconnection are approximately
 315 balanced, which we term *driven phases* (L, N, V). This occurs if the IMF remains south-
 316 wards and $\Phi_D^* > 10$ kV following the initial substorm bay in AL. This period may last

317 for a few 10s of minutes or many hours, depending on the variability of the IMF. Dur-
 318 ing these periods, Λ , PCN, AU and AL remain approximately constant. Typically, $|\text{AL}| \approx$
 319 AU, though AL may also show negative excursions.

320 Lockwood et al. (2009) referred to such phases as steady convection events (SCEs)
 321 and likened them to periods of steady magnetospheric convection (SMC). In previous
 322 studies, periods of SMC are usually identified as having very steady AL over a minimum
 323 duration of several hours. In this study, we allow AL to vary somewhat, that is to en-
 324 compass periods when intensifications in nightside reconnection may be ongoing. DeJong
 325 (2014) studied periods of SMC with steady and non-steady AL and concluded that these
 326 represent periods of weaker and stronger solar wind driving.

327 During driven phases $\Phi_D \approx \Phi_N$ and F_{PC} is relatively constant, such that they
 328 have been referred to as balanced reconnection intervals (DeJong et al., 2008). However,
 329 there is no direct constraint on Φ_N that it exactly equals Φ_D , and slow changes in Φ_D
 330 can result in a mismatch between the two, leading to gradual variations in F_{PC} ; we term
 331 this *quasi-balanced reconnection*. Occasionally, a gradual expansion in the polar cap dur-
 332 ing a driven phase can lead to an onset-like AL bay and a subsequent decrease in Λ . We
 333 note the time of these *driven phase onsets* for later analysis (though they are not con-
 334 sidered to be a state category in themselves). Three such events have been represented
 335 as red vertical dashed lines during intervals M and V.

336 **2.2.6 Multiple intensifications**

337 Some driven phases during periods of strong solar wind coupling are characterised
 338 by large quasiperiodic negative excursions of AL, with a periods of 30-60 min. It is un-
 339 clear if these represent individual substorms or are intensifications of the on-going night-
 340 side reconnection. The period of these intensifications is sufficiently short that no coher-
 341 ent expanding/contracting behaviour is seen in Λ , which remains relatively constant. We
 342 identify these as intervals of *multiple intensifications* (M). Such periods, when rapid changes
 343 in magnetic perturbations are observed on the ground, are those most likely to give rise
 344 to damaging space weather effects on ground-based infrastructure.

345 **2.2.7 Recovery bays**

346 Occasionally, the recovery phase at the end of a driven phase can be accompanied
 347 by an AL bay. Sergeev et al. (1996) noted that many SMC begin and end with a sub-
 348 storm, and Milan et al. (2019) noted that a substorm-like signature could accompany
 349 a northward turning of the IMF at the end of a period of SMC. We identify these pe-
 350 riods as *recovery bays* (D, O).

351 **2.2.8 Weak activity**

352 During periods of relatively weak solar wind driving, $\Phi_D^* < 10$ kV, AU, AL and
 353 PCN can be slightly elevated, $\text{AU} \approx -\text{AL} \approx 50$ nT. However, no other coherent features
 354 are seen that identify the periods as growth, expansion, driven, or recovery phases. Also,
 355 often the R1/R2 FACs are too weak for Λ to be measured reliably. We refer to these as
 356 periods of *weak activity* (X).

357 **3 Results and discussion**

358 In the 360 full days of data that are included in the analysis, just under 3500 cat-
 359 egory boundaries and 196 driven phase onsets are identified. This dataset is available
 360 as Milan (2020). First we discuss the characteristics of each category, and then sequences
 361 of categories.

Table 1. Number and duration of each convection state category

Category	Number	Duration		
		Total (h)	Total (%)	Event (h)
Quiescent	799	3971.6	46.0	4.97
Weak activity	234	735.4	8.5	3.14
Growth phase	752	976.3	11.3	1.30
Expansion	568	470.0	5.4	0.83
Driven	447	1582.4	18.3	3.54
Recovery	502	559.3	6.5	1.11
Recovery bay	176	227.5	2.6	1.29
Multiple intensifications	12	119.3	1.4	9.94

Table 2. Average parameters during convection state categories

Category	Φ_D^* (kV)	PCN (nT)	AU (nT)	AL (nT)	SYM-H (nT)	Total $\int \Phi_D^*$ (GWb)	$\int \Phi_D^*$ (%)	ΔF_{PC} (GWb)
Quiescent	3.2	0.2	18.3	-16.7	-4.6	43.3	13.3	0.057
Weak activity	7.7	0.5	31.8	-40.7	-7.3	20.3	6.0	0.087
Growth	20.1	0.7	44.4	-46.1	-7.1	70.7	20.8	0.094
Expansion	19.6	1.1	66.8	-179.9	-10.4	33.2	9.8	0.059
Driven	22.5	1.2	77.7	-151.9	-14.9	128.1	37.6	0.287
Recovery	5.6	0.8	64.3	-99.8	-13.9	11.3	3.3	0.023
Recovery bay	4.8	0.8	61.7	-143.1	-11.9	3.9	1.2	0.022
Multiple intensifications	63.7	2.5	214.7	-522.6	-50.5	27.4	8.0	2.279

3.1 Convection state statistics

Table 1 summarises the number of each category, the total duration in terms of hours and percentage of the whole year, and the average duration of each event. Table 2 summarises the characteristics of the events, including average Φ_D^* , PCN, AU, AL, and SYM-H. Also shown is the total amount of open flux created by dayside reconnection during each category, $\int \Phi_D^* dt$, in terms of GWb and as a percentage over the year, and as event averages, which we refer to as ΔF_{PC} .

Quiescent periods account for almost half of the year, corresponding to periods when IMF $B_Z > 0$. There were almost 800 quiet periods, with an average duration of 5 h, though this duration is very variable. Although we expect little dayside coupling during these events, Φ_D^* is a non-negative number and 13% of the estimated open flux accumulated by the magnetosphere over the course of the year occurs in this 46% of the time, though at an average rate of only 3.2 kV. AL, AU, and SYM-H are low during these periods. Weak activity is driven by $\Phi_D^* \approx 8$ kV for 9% of the time, with an average duration of 3.1 h, and accounts for 6% of the accumulated open flux over the year.

Growth, expansion, and driven phases have on average $\Phi_D^* \approx 20$ kV, and last approximately 1 h. As expected, during growth phases $|AL| \approx AU$; $|AL| > AU$ during expansion and driven phases, by a factor of 2.5 and 2, respectively. 21% of the open flux of the magnetosphere is accumulated during growth phases, whereas expansion and driven phases account for 10% and 38% of the flux throughput, respectively. The magnetosphere is in a driven state for 18% of the time, expansion and recovery phases accounting for 6% each.

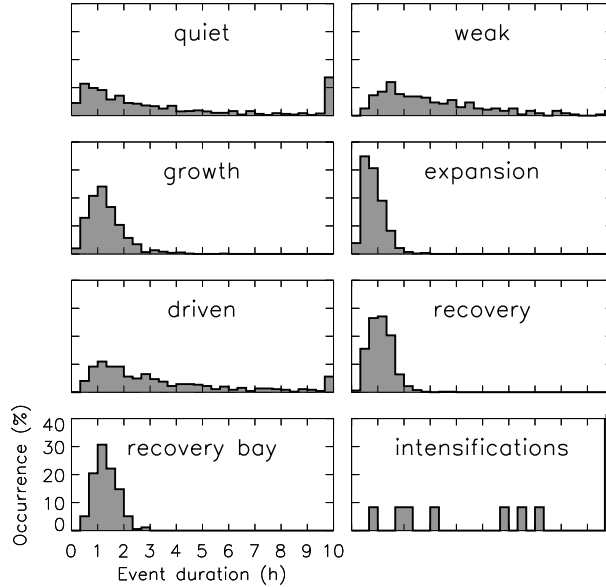


Figure 4. Distributions of event durations for each category, in bins of 20 min. The rightmost bin shows the number of events that exceed a duration of 10 h.

384 On average $\Phi_D^* \approx 5$ kV during recovery and recovery bay phases. However, the
 385 flux closed by tail reconnection during these events must account for the flux opened dur-
 386 ing growth and expansion phases (assuming reconnection is approximately balanced dur-
 387 ing driven phases). The only parameter that apparently distinguishes between recovery
 388 phases with and without bays is the magnitude of AL.

389 The distribution of event duration for each category is presented in Figure 4. The
 390 distributions for growth, recovery, and recovery bay phases are all similar, peaking near
 391 1 h (and median 1 h). This suggests that they represent the timescales over which mag-
 392 netic flux is opened and closed prior to or following the establishment of a NENL. The
 393 expansion phase distribution is also similar, though peaks near 30 min (median 40 mins),
 394 and represents the timescale over which the magnetotail establishes this new NENL in
 395 response to open flux being accumulated in the magnetotail lobes. The quiet, weak, and
 396 driven phases also have distributions that resemble each other, though these are much
 397 broader (median 2 h). We interpret these as reflecting the variability of IMF B_Z , being
 398 the distributions of waiting times between significant north-south and south-north turn-
 399 ings of the IMF. Multiple intensifications have a distribution with a median of 5 h, pre-
 400 sumably representing the timescale of intense storm periods.

401 The left panels of Figure 5 show distributions of IMF B_Y and B_Z for each category.
 402 In the main, $\sqrt{B_Y^2 + B_Z^2} < 15$ nT in these distributions. All the distributions are
 403 approximately symmetric in IMF B_Y , though there was a slight tendency for $B_Y < 0$
 404 (and $B_X > 0$) to dominate in 2010. The quiet distribution maximises for $B_Z > 0$, though
 405 short periods of $B_Z < 0$ also occur owing to the high frequency variability of the solar
 406 wind. Weak activity periods are associated with $B_Z \approx 0$. Growth phases are pre-
 407 dominantly associated with $B_Z < 0$, as expected, though there are also brief periods
 408 of $B_Z > 0$ due to the variability of the solar wind. The expansion and driven phase dis-
 409 tributions are the same as for growth phases. This indicates that growth, expansion, and
 410 driven phases are produced by the same solar wind driving conditions, and the demar-
 411 cation into these different phases is due to the past activity within the magnetosphere
 412 and the natural evolution of substorms (e.g. growth to expansion to recovery). Recov-

413 ery and recovery bay phases both have distributions that resemble quiet phases (i.e. no
414 or low solar wind driving).

415 The IMF B_X-B_Y distributions (not shown) for the different categories are in gen-
416 eral consistent with a Parker spiral configuration ($B_X \approx -B_Y$). Periods of multiple in-
417 tensifications are unlike this, however, being dominated by a southward B_Z component,
418 and an average $\Phi_D^* > 60$ kV. These periods also have enhanced SYM-H with an av-
419 erage value of -50 nT. They only account for 1% of the year, but produce 8% of the open
420 flux throughput of the magnetosphere.

421 The middle panels of Fig. 5 show the distributions of solar wind velocity and num-
422 ber density during each category. In 2010, the solar wind varied between periods of high
423 solar wind speed and low solar wind density and periods of low speed and highly vari-
424 able density (see also Section 3.4). $V_{SW} \approx 450$ km s⁻¹ can be viewed as an approxi-
425 mate demarcation between the two types of solar wind (vertical grey line). The value
426 in the top right of each panel is the fraction of the distribution that falls in the fast so-
427 lar wind regime. 81% of quiet and 73% of weak activity occur during slow solar wind.
428 Growth, expansion, driven, and recovery phases occur between 66% and 59% during slow
429 solar wind; recovery bays are equally distributed between fast and slow wind. Multiple
430 intensifications, however, occur 68% during fast solar wind.

431 The right panels of Fig. 5 show distributions in SYM-H and Λ . An increase in Λ
432 with more negative SYM-H is apparent in many of the distributions, as described by Milan,
433 Hutchinson, et al. (2009) and Milan (2009). A diagonal line, $\Lambda = 17 - \text{SYM-H}/8$, has
434 been superimposed to aid discussion. Most distributions peak in the range $-20 > \text{SYM-}$
435 $\text{H} > 0$ and $18 < \Lambda < 20^\circ$, which comprises moderately disturbed conditions. Both
436 quiet and weak activity categories have a significant extension to lower Λ . As Λ increases
437 the trend to more negative SYM-H is clear, especially for driven and recovery phases.
438 The distribution for multiple intensifications appears to be a high- Λ extension of the driven
439 phase distribution (in agreement with Milan et al. (2019)). The growth and expansion
440 phase distributions cut off above $\Lambda \approx 25^\circ$, whereas the driven and multiple intensifi-
441 cations distributions extend to 28° . The majority of the expansion phase distribution
442 falls above the superimposed diagonal line, the driven phase falls on it, and the recov-
443 ery phases fall below it: this is consistent with the discussion of Milan, Hutchinson, et
444 al. (2009) regarding the temporal evolution of magnetospheric state during disturbed pe-
445 riods. Finally, we note that the growth phase distribution contains a population with
446 positive SYM-H; as will be discussed in Section 3.2, many growth phases appear to oc-
447 cur at the transition from slow, high-density solar wind (when the magnetopause is com-
448 pressed) to fast, low-density wind (when dayside driving increases).

449 3.2 Sequence statistics

450 We now turn to a discussion of the temporal evolution of the system. We can search
451 for particular sequences of categories in our list: for instance, a “classic” isolated sub-
452 storm would comprise the categories quiet then growth, followed by expansion, recov-
453 ery, and finally quiet (Q-G-E-R-Q). In Figure 6 we perform a superposed epoch anal-
454 ysis of state parameters during the following sequences: (a) Q-W-Q, (b) Q-G-R-Q, (c)
455 Q-G-E-Q, (d) Q-G-E-R-Q, (e) Q-G-E-D-Q, (f) Q-G-E-D-R-Q, (g) Q-G-E-D-RB-Q, where
456 W, D, and RB refer to weak activity, driven phases, and recovery bays. The zero epoch
457 is the end of the initial quiet phase. The time axis is constructed so that the duration
458 of each category is normalised to its average within the ensemble. Only one hour of the
459 preceding and following quiet periods is shown, though in practice these may be longer.

460 Case (a) represents an interval of weak driving amongst otherwise quiet conditions.
461 This is marked by $\Phi_D^* \approx \Phi_{PC}^* \approx 7$ kV and $\text{AU} \approx -\text{AL} \approx 40$ nT over a period of 3 h.
462 Λ rises from 16° during the quiet periods to 17° during the weak activity.

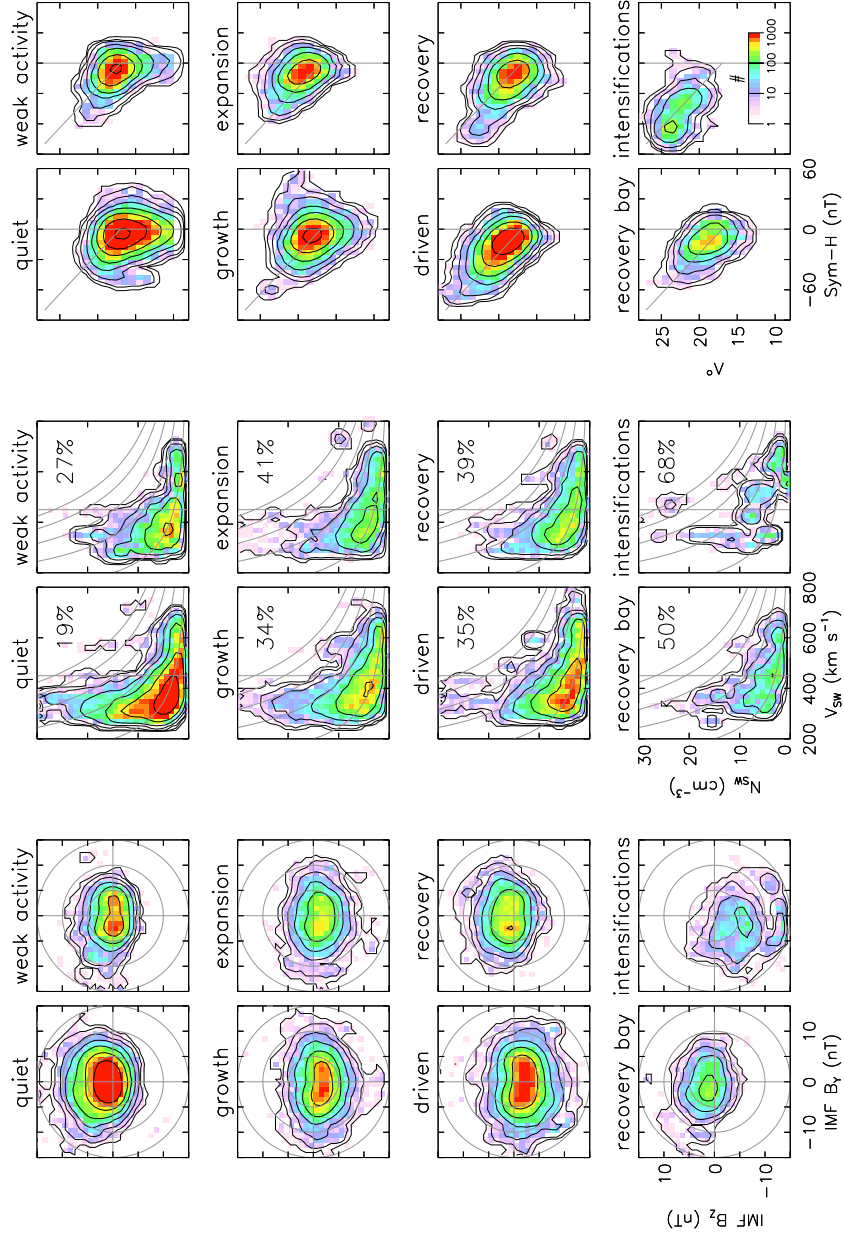


Figure 5. (Left) Occurrence distributions of the IMF B_Y and B_Z components during each category, on a log scale. (Middle) Distributions of solar wind speed, V_{SW} , and density, N_{SW} . Grey curves show locii of solar wind ram pressure of 1, 3, 5, 7, and 9 nPa. The vertical grey line shows an approximate demarcation between slow and fast solar wind; the fraction of the distribution that is associated with fast solar wind is shown in the top right. (Right) Distributions of SYM-H and FAC radius, Λ . A diagonal grey line, $\Lambda = 17 - \text{SYM-H}/8$, is added for reference.

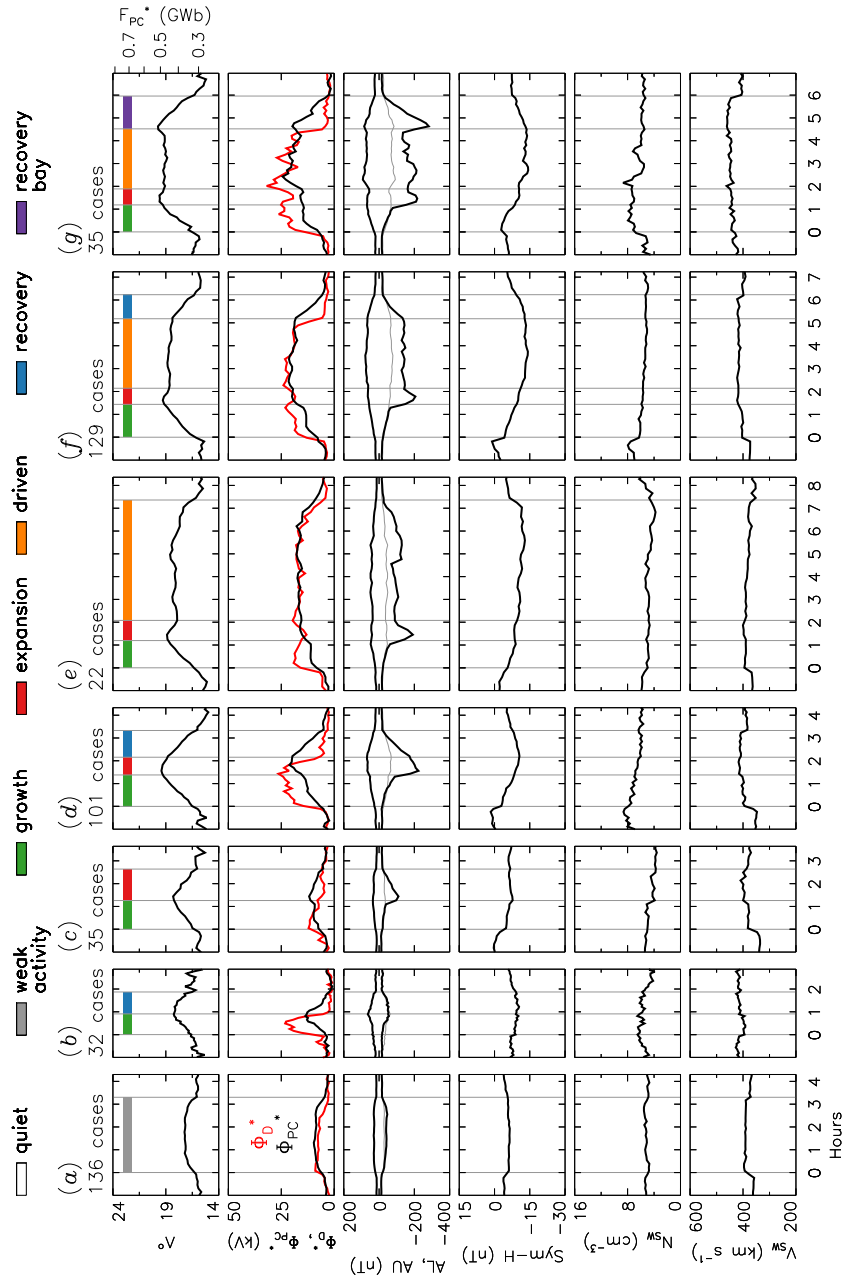


Figure 6. Superposed epoch analyses of different sequences of categories (see text for details). In each case the duration of each category has been normalised to the average duration of the ensemble.

463 Next we discuss case (d), the classic isolated substorm. Reconnection switches on
 464 with $\Phi_D^* \approx 20$ kV, and during the ensuing growth phase lasting just over an hour the
 465 polar cap expands to $\Lambda \approx 20^\circ$. AL and AU increase in magnitude through this phase,
 466 with $AU \approx -AL$ indicating that the strengths of the eastward and westward electro-
 467 jets are comparable, and no substorm electrojet is present. Substorm onset then occurs,
 468 with a sudden negative excursion of AL to -200 nT, marking the formation of the sub-
 469 storm electrojet. Dayside reconnection is still ongoing at this stage but eventually ceases
 470 with a northward turning of the IMF, after 50 mins on average. The magnetosphere en-
 471 ters recovery phase, and the polar cap contracts and AU and AL return to quiet time
 472 values over the course of 70 mins. Through this sequence we expect that $\Phi_D > 0$, $\Phi_N =$
 473 0 during the growth phase, $\Phi_D > 0$, $\Phi_N > 0$ during the expansion phase, and $\Phi_D =$
 474 0 , $\Phi_N > 0$ during the recovery phase. As discussed in the introduction, we expect Φ_{PC}
 475 to approximate a smoothed moving average of Φ_D and Φ_N , and indeed this is the ob-
 476 served behaviour of Φ_{PC}^* .

477 Case (b) represents a period of dayside reconnection, $\Phi_D^* \approx 20$ kV, during which
 478 the polar cap expands to $\Lambda \approx 18^\circ$; however, before a substorm is triggered dayside driv-
 479 ing ceases, the magnetosphere enters a recovery phase and the polar cap contracts. AU/AL
 480 increase and then decrease, but without the formation of a substorm bay. Case (c) rep-
 481 represents a growth phase followed by substorm onset, but in which the dayside driving is
 482 weak, $\Phi_D^* \approx 10$ kV, and decreases following onset such that expansion and recovery phases
 483 appear combined.

484 We now discuss (f), in which dayside driving remains high beyond the point that
 485 the substorm bay has begun to diminish. During this driven phase, $\Phi_N \approx \Phi_D$, Λ re-
 486 mains uniform, and the magnitude of AL exceeds that of AU, but not as much as dur-
 487 ing expansion phase. Eventually, after approximately 3 h on average, dayside driving ceases,
 488 but ongoing nightside reconnection leads to a recovery phase during which Λ decreases.
 489 Throughout, Φ_{PC} is a smoothed moving average of Φ_D and Φ_N , as expected. Case (g)
 490 is similar, but the recovery phase associated with the northward turning of the IMF is
 491 accompanied by a significant substorm-like bay. Case (e) is also similar, but rather than
 492 an abrupt cessation of dayside driving marking the end of the driven phase, Φ_D decreases
 493 gradually, as do Φ_N , Φ_{PC} and Λ , that is, the driven phase peters out without the oc-
 494 currence of a clear recovery phase.

495 In Figure 7 (a) to (c) we repeat the same analysis for Q-G-E-R-Q sequences (iso-
 496 lated classic substorms), except we subdivide the events by the size of the polar cap at
 497 the time of expansion phase onset: $\Lambda = 16 - 18^\circ$, $18 - 20^\circ$, and $20 - 22^\circ$ (indicated by
 498 the red boxes in the upper panels). Substorms with greater Λ at onset are driven by larger
 499 Φ_D^* during the growth phase, have higher Φ_{PC}^* , and are more intense as measured in AL,
 500 all results consistent with previous findings (Milan, Grocott, et al., 2009; Clausen et al.,
 501 2013; Coxon et al., 2014).

502 Fig. 7 (d) to (f) show the same analysis for Q-G-E-D-R/RB-Q sequences (substorms
 503 with a driven phase, and ending in either a recovery phase or recovery bay), again sub-
 504 divided by Λ at onset. The growth and expansion phases behave similarly to the isolated
 505 substorms, which is to be expected as the subsequent activity (driven phase or not) is
 506 determined by the behaviour of the IMF after onset. We find that Λ during the driven
 507 phase is dependent on the preceding behaviour, that is the polar cap is larger during more
 508 strongly driven events.

509 Examining the behaviour of SYM-H in Fig. 7, we note that it starts near 0 dur-
 510 ing the quiet period, decreases during the growth and expansion phases (more-so dur-
 511 ing strongly driven substorms), and plateaus during a subsequent driven phase. It is pos-
 512 sible that Λ during the driven phase is controlled by SYM-H, as proposed by Milan, Hutchin-
 513 son, et al. (2009). For both substorms with and without a driven phase, the more strongly
 514 driven cases appear on average to have a step in solar wind density near the start of the

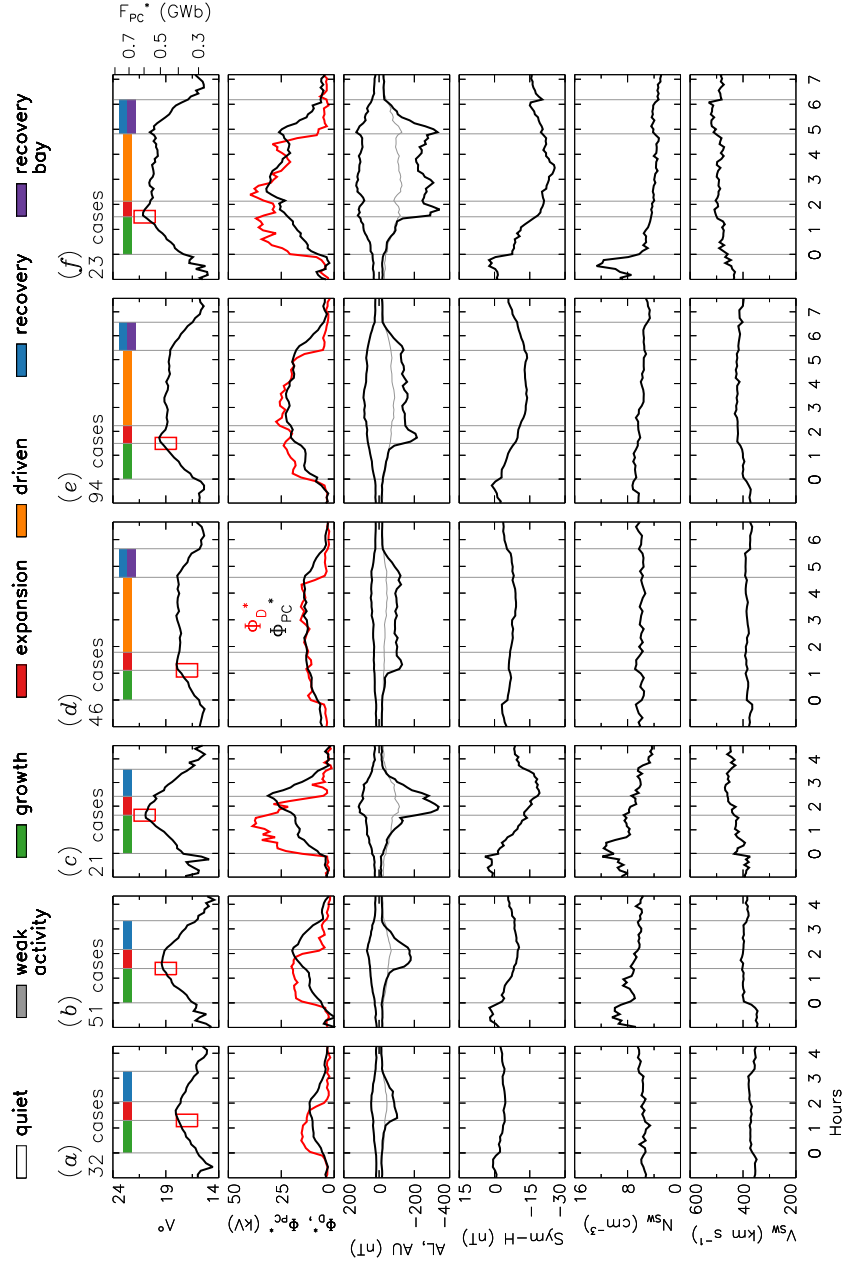


Figure 7. Superposed epoch analyses of growth-expansion-recovery and growth-expansion-driven-recovery sequences (see text for details). These are repeated three times for expansion phases that commence for $16 < \Lambda < 18^\circ$, $18 < \Lambda < 20^\circ$, and $20 < \Lambda < 22^\circ$ (indicated by the red boxes).

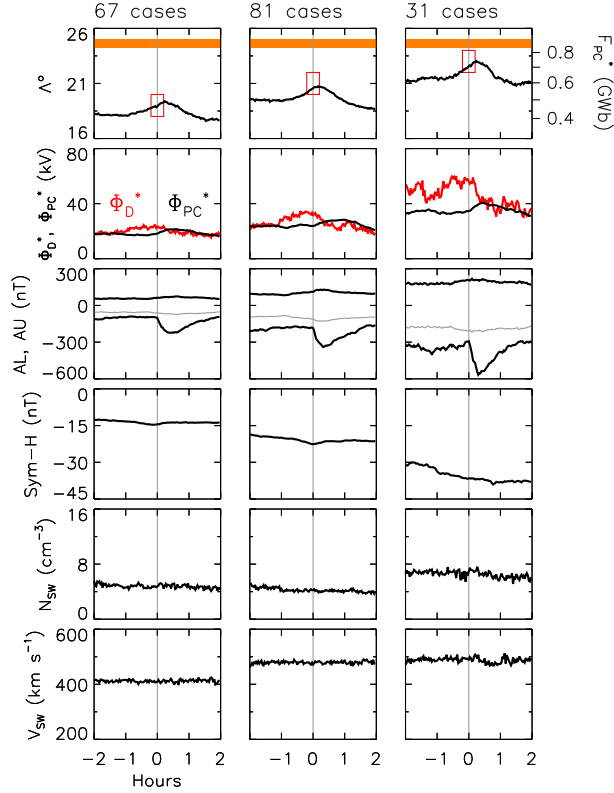


Figure 8. Superposed epoch analyses of driven phase onsets from two hours before to two hours after onset. This is repeated three times for onsets for which $18 < \Lambda < 20^\circ$, $20 < \Lambda < 22^\circ$, and $22 < \Lambda < 24^\circ$ (indicated by the red boxes).

515 growth phase (also apparent as a simultaneous positive excursion of SYM-H). We also
 516 note that more weakly and more strongly driven cases are on average associated with
 517 lower (350 km s^{-1}) and higher (500 km s^{-1}) solar wind speed, respectively.

518 In many of the substorms identified in Fig. 3, F_{PC}^* continues to grow for 20 mins
 519 or so after expansion phase onset. This behaviour is also seen in some of the superposed
 520 epoch analyses of Fig. 6. On one hand, in most cases Φ_D^* remains high after onset, so
 521 open flux continues to be accumulated even after nightside reconnection has commenced,
 522 and if $\Phi_D > \Phi_N$ then F_{PC} will continue to grow. On the other hand, the assumption
 523 that the polar cap is circular, used to calculate F_{PC}^* , is likely to break down at these times
 524 due to the formation of a substorm auroral bulge (Mooney et al., 2020), and it is possi-
 525 ble that F_{PC}^* overestimates the true polar cap flux during the expansion phase.

526 3.3 Driven phase onsets

527 As mentioned in Section 2.2.5, there is an additional category of substorm-like onset
 528 that can occur during prolonged driven phases. These driven phase onsets are stud-
 529 ied in Figure 8, which presents superposed-epoch analyses from 2 h before to 2 h after
 530 these onsets; these have been subdivided by $\Lambda = 18 - 20^\circ$, $20 - 22^\circ$, and $22 - 24^\circ$ at
 531 onset (delineated by the red boxes in the upper panels). In total, 196 such events were
 532 identified in this study (on average one for every 10 h of driven phase duration over the
 533 course of the year).

534 Driven phases are periods of quasi-balanced dayside and nightside reconnection,
 535 $\Phi_N \approx \Phi_D$ and $F_{PC} \approx \text{const}$, that is, periods during which the magnetotail has adjusted
 536 itself to release magnetic flux at the same rate that it is being accumulated on the day-
 537 side. However, Φ_D responds promptly to changes in the solar wind, whereas Φ_N appears
 538 to respond more slowly. For instance, an abrupt northwards turning of the IMF can lead
 539 to a sudden decrease in Φ_D but nightside reconnection can continue unabated, result-
 540 ing in a decrease in F_{PC} (which we define as a recovery phase).

541 Driven phase onsets appear to be the response to more gradual changes in Φ_D , specif-
 542 ically moderate increases. Fig. 8 shows that on average 2 h prior to each onset $\Phi_D^* \approx$
 543 Φ_{PC}^* , but that a slight increase in Φ_D^* occurs approximately 1 h before. Φ_{PC}^* remains
 544 unchanged at this time, suggesting that Φ_N also continues uniformly. Dayside and night-
 545 side reconnection are now slightly unbalanced leading to an increase in F_{PC} (Λ). Even-
 546 tually this situation can no longer be supported and onset occurs: Λ decreases and Φ_{PC}^*
 547 increases, accompanied by a bay in AL, all lasting approximately 90 mins. These obser-
 548 vations suggest that Φ_N has suddenly increased to exceed Φ_D for the duration of these
 549 90 min, accompanied by the formation of a substorm current wedge, presumably asso-
 550 ciated with a new NENL.

551 After 90 mins, Φ_D and Φ_N are balanced once again. Indeed, the increase in Φ_D^*
 552 that triggers the onset is reversed shortly after onset, on average. We interpret this as
 553 being due to the natural short-term variability of the IMF, coupled with the fact that
 554 enhanced Φ_D is no longer necessary to trigger a driven phase onset. This is essentially
 555 the same argument put forward by Freeman and Morley (2004) for explaining the ap-
 556 parent association between substorm onsets and northwards turnings of the IMF in su-
 557 perposed epoch analyses (e.g., Caan et al., 1977; Lyons, 1995).

558 We have argued that classic substorms are those that occur within an hour or so
 559 of a southward turning of the IMF, and for which the IMF turns northwards again shortly
 560 after onset. The expansion phase of these substorms marks the establishment of a NENL
 561 and the formation of a substorm current wedge, which produces a bay in AL, in response
 562 to the accumulation of open magnetic flux in the magnetotail. If the IMF remains south-
 563 wards for a significant period, the magnetosphere can segue from substorm expansion
 564 phase to what we have termed the driven phase, when dayside and nightside recon-
 565 nection are balanced. Within these driven phases, modest increases in the dayside recon-
 566 nection rate can result in a further accumulation of open flux in the magnetotail, lead-
 567 ing to a driven phase onset, again accompanied by a bay in AL. Our interpretation is
 568 that during driven phases the NENL has evolved into a DNL. Subsequent increases in
 569 magnetotail flux may trigger the formation of a new NENL and SCW, leading to the driven
 570 phase onset bay. Hence, we identify driven phase onsets and classic substorms with in-
 571 tervals of NENL formation when a DNL is active or absent down-tail, respectively. The
 572 near-Earth tail dynamics that occur during these two types of event are essentially the
 573 same, but occur within the context of differing magnetospheric convection, and subse-
 574 quently contribute towards that convection. Hence, what are referred to as the “directly-
 575 driven” and “loading-unloading” aspects of magnetospheric activity – or the “two-component
 576 auroral electrojets” (Kamide & Kokubun, 1996) – are two sides of the same coin.

577 Finally, we note that the higher Λ cases occur during periods of higher magnitude
 578 SYM-H, again consistent with the suggestion that ring current intensity modulates the
 579 stability of the magnetotail to the onset of reconnection in the near-Earth tail (Milan,
 580 Hutchinson, et al., 2009). In addition, higher Λ cases are associated with higher solar
 581 wind speeds.

582 Besides the onsets described above, there are often substorm-like bays in AL dur-
 583 ing driven phases that do not appear associated with changes in solar wind conditions
 584 or significant variations in F_{PC} . DeJong (2014) also noted the variability of AL during
 585 strongly driven SMC periods, and Milan et al. (2006) reported multiple tail dipolarisa-

586 tions during a substorm prolonged by ongoing dayside reconnection. These fluctuations
 587 are most intense during periods of multiple intensifications, which are associated with
 588 the largest values of Λ . It is unclear what these fluctuations represent – a rapidly reform-
 589 ing NENL, repeated intensifications of an active NENL, or some other explanation – and
 590 this requires further study.

591 3.4 Relation to solar wind structure and variability

592 In section 3.1 we investigated the solar wind conditions during different convection
 593 categories. The differences between the $N_{SW}-V_{SW}$ distributions was not great, though
 594 quiet periods were predominantly found during slow solar wind conditions. This can be
 595 understood through the V_{SW} contribution to Φ_D^* in eq. (5): slow solar wind in general
 596 leads to low Φ_D^* unless a solar wind structure leads to unusually high IMF magnitude.

597 2010 comprised repeating periods of fast solar wind with low density followed by
 598 slow solar wind with highly variable density. Figure 9 shows two such intervals, compris-
 599 ing days-of-year (DOYs) 164 to 194 and 281 to 311. The upper panel shows the fraction
 600 of each day occupied by different states; the next panel shows the open flux accumulated
 601 by dayside reconnection during each day, broken down by category. Below this are the
 602 times of onsets of expansion phases (red ticks) and driven phase onsets (blue ticks), Λ° ,
 603 IMF B_Z , V_{SW} and N_{SW} , AU and AL, and SYM-H. We note the anti-correlation between
 604 SYM-H and Λ , previously reported by Milan, Hutchinson, et al. (2009).

605 Prolonged quiet periods are associated with slow solar wind (DOY 170-172, 186-
 606 188, 287, 303-305) and/or extended IMF $B_Z > 0$ (DOY 172, 304-305). Conversely, pe-
 607 riods of high flux transport can be associated with fast solar wind (DOY 167, 180-184,
 608 296-297). Some periods of high Φ_D^* occur after steps in solar wind density, when the so-
 609 lar wind may be slow but the IMF is compressed and has a relatively high magnitude
 610 (DOY 190, 284-285); such periods contribute to the high solar wind density seen at the
 611 start of growth phases as discussed in relation to Figs. 6 and 7. Other periods have mod-
 612 erately high solar wind speed but low Φ_D^* (DOY 300-301) because the B_Z component
 613 of the IMF is of low magnitude.

614 In addition, although the general solar wind conditions may be similar during two
 615 different periods, the nature of the coupling can vary: for instance, compare DOY 180-
 616 184, when most flux transport occurs during driven phases, with DOY 295-299, when
 617 expansion phases dominate. In the latter case the B_Z component of the IMF oscillated
 618 north-south with a period of a few hours, leading to multiple isolated substorms, whereas
 619 $B_Z < 0$ was more sustained during the former period.

620 We conclude that the detailed nature of convection is determined by the details of
 621 relatively short-lived variations in the solar wind and IMF, within an overarching expect-
 622 ation that prolonged periods of high and low solar wind speed tend to lead to stronger
 623 and weaker convection.

624 4 Conclusions

625 Using proxies for the dayside reconnection rate, Φ_D^* , cross-polar cap potential, Φ_{PC}^* ,
 626 open magnetic flux, F_{PC}^* , and the electrojet indices, AU and AL, we have identified con-
 627 vection state continuously throughout 2010. The states we identify are: quiet (which oc-
 628 curs 46% of the time and accounts for 13% of the magnetic flux throughput of the mag-
 629 netosphere), weak activity (9%, 6%), the substorm phases of growth (11%, 21%), expan-
 630 sion (5%, 10%), driven (18%, 38%), and recovery (8%, 5%), and storm periods compris-
 631 ing multiple intensifications (1%, 8%).

632 The driven phase occurs after substorm expansion phase if the IMF remains south-
 633 wards for a prolonged period, and ends with the subsequent northward turning. This rep-

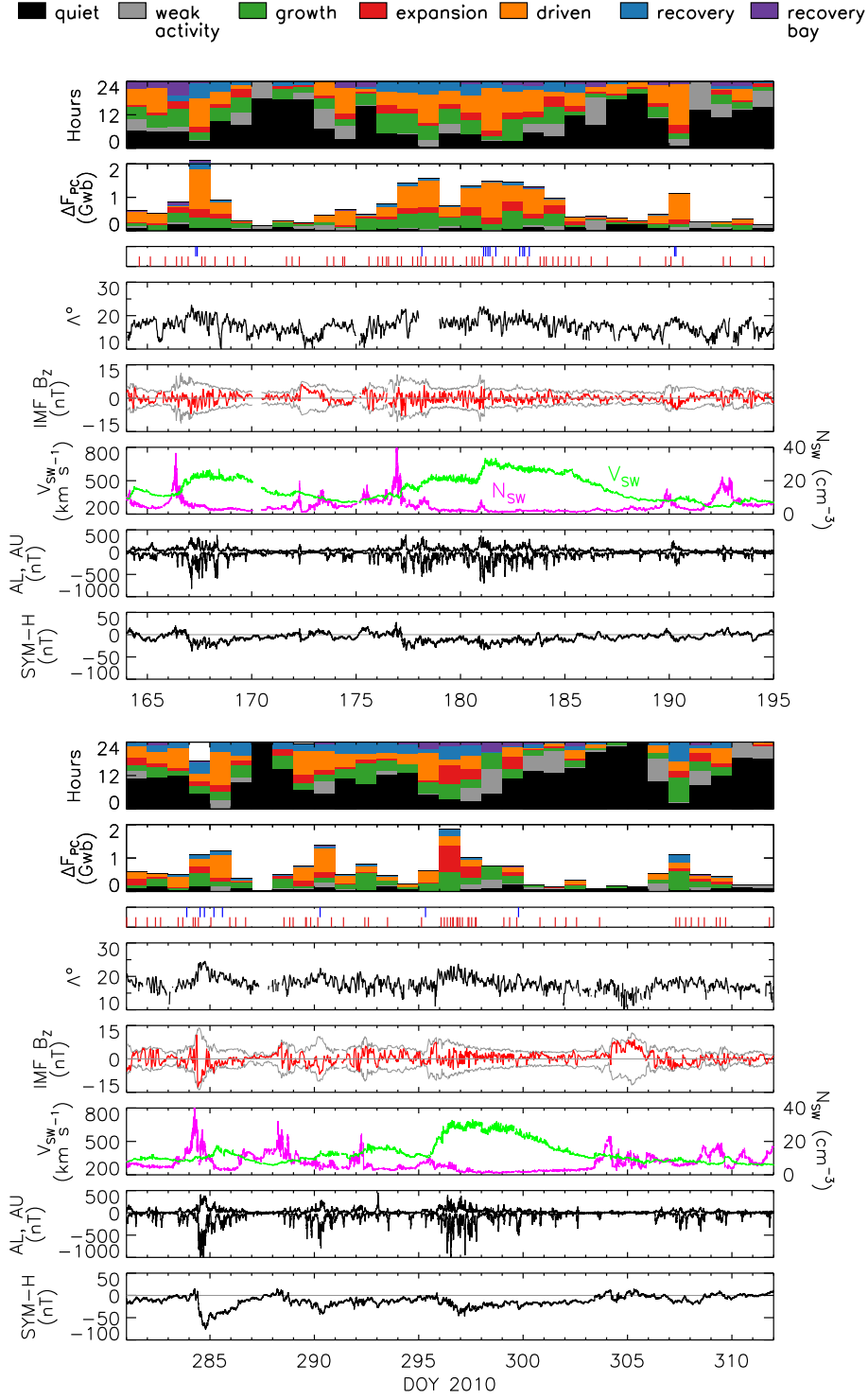


Figure 9. A comparison of two 31-day periods from 2010, showing broadly similar solar wind speed and density structures. The upper two panels show the fraction of each day occupied by different convection categories and the amount of open flux accumulated by dayside reconnection during each category (ΔF_{PC}). Red and blue ticks show the times of expansion phase onsets (red) and driven phase onsets (blue). In the IMF B_Z panel, the grey curves show the envelope of the total IMF magnitude.

634 represents intervals when the nightside reconnection rate is quasi-balanced with the day-
 635 side rate such that the magnetosphere enters a state of steady convection. Following a
 636 cessation of dayside driving, the nightside rate remains elevated for an hour or so, lead-
 637 ing to the recovery phase. During these driven phases, modest variations of Φ_D can lead
 638 to slight imbalances with Φ_N which result in gradual variations in F_{PC} . In the case of
 639 $\Phi_D > \Phi_N$, a gradual increase in F_{PC} can lead to a new substorm onset, signalled by
 640 an AL bay and an abrupt enhancement in Φ_N leading to a decrease in F_{PC} ; thereafter,
 641 the driven phase can continue. We refer to these as driven phase onsets.

642 Besides driven phase onsets, there can be significant bay-like activity in AL dur-
 643 ing driven phases, but without attendant variations in F_{PC} . The cause of these bays is
 644 not yet understood, but they could be reformations of the NENL or re-intensifications
 645 of already ongoing tail reconnection. Further work is necessary to identify the nature of
 646 these onsets.

647 In our scheme, we identify growth phases as periods of dayside but no nightside
 648 reconnection, expansion phases as the onset of nightside reconnection at a near-Earth
 649 neutral line, we assume driven phases occur once the NENL has progressed down-tail
 650 to form a distant neutral line, and recovery phases as ongoing DNL reconnection after
 651 dayside reconnection has ceased. We interpret driven phase onsets as the formation of
 652 a new NENL whilst a DNL is already active. This provides a framework for understand-
 653 ing the difference between isolated substorms and those occurring during ongoing activ-
 654 ity. Isolated substorms are associated with brief southward turnings of the IMF. Longer
 655 periods of driving result in substorm driven phases, during which driven phase onsets
 656 can occur. This framework encompasses the two-component auroral electrojet model of
 657 Kamide and Kokubun (1996).

658 The size of the polar cap is strongly influenced by SYM-H. As speculated in pre-
 659 vious studies (e.g., Milan, Hutchinson, et al., 2009; Milan, 2009), we suggest that the cri-
 660 terion for reconnection onset in the tail is a balance between two competing factors: thin-
 661 ning of the plasma sheet by the pressure produced by inflated lobes (hence a growth phase
 662 being required prior to onset), and the magnetic perturbation introduced by the ring cur-
 663 rent into the magnetotail which counteracts the thinning. The magnitude of SYM-H then
 664 controls the value of F_{PC} required for substorm onset and the equilibrium level of F_{PC}
 665 during driven phases. Fig. 7 indicates that SYM-H grows during the growth phase at
 666 a rate that is controlled by Φ_D . This in turn dictates the size of the polar cap at the time
 667 of substorm onset. SYM-H and F_{PC} plateau during any subsequent driven phase. SYM-
 668 H then controls the level of F_{PC} required for driven phase onsets to occur.

669 Approximately a quarter of recovery phases are associated with a bay in AL, which
 670 we refer to as recovery bays. The nature and cause of these recovery bays is not yet clear
 671 and will be investigated in future work, including a comparison with the bays associated
 672 with substorm onsets, driven phase onsets, and other bay-like activity in AL.

673 In this study we have analysed magnetospheric state for the duration of the year
 674 2010, the beginning of solar cycle 24. Due to the relative complexity of the task, the clas-
 675 sification was done by hand (a somewhat labourious undertaking). However, AMPERE
 676 data is currently available for the period 2010 to 2016, encompassing the rising phase
 677 and maximum of the solar cycle, providing a means to study in detail the long-term in-
 678 fluence of solar activity on magnetospheric convection. We hope to use the dataset we
 679 have produced so far to develop an automated procedure to extend the classification to
 680 the whole seven-year interval.

681 Acknowledgments

682 SEM and JAC were supported by the Science and Technology Facilities Council (STFC),
 683 UK, grant no. ST/S000429/1; HS and GB were supported by STFC studentships. The

684 work at the Birkeland Centre for Space Centre, University of Bergen, Norway, was sup-
 685 ported by the Research Council of Norway/CoE under contract 223252/F50. We thank
 686 the AMPERE team and the AMPERE Science Center for providing the Iridium-derived
 687 data products; AMPERE products are available at <http://ampere.jhuapl.edu>. The
 688 AMPERE FAC radii dataset is available at [https://doi.org/10.25392/leicester.data](https://doi.org/10.25392/leicester.data.11294861.v1)
 689 [.11294861.v1](https://doi.org/10.25392/leicester.data.11294861.v1). The convection state data accompanying this paper is available at [https://](https://doi.org/10.25392/leicester.data.12571307.v1)
 690 doi.org/10.25392/leicester.data.12571307.v1. The OMNI data, including solar
 691 wind parameters and geomagnetic indices, were obtained from the GSFC/SPDF OM-
 692 NIWeb interface at <http://omniweb.gsfc.nasa.gov>.

693 References

- 694 Anderson, B., Takahashi, K., Kamei, T., Waters, C., & Toth, B. (2002). Birkeland
 695 current system key parameters derived from Iridium observations: Method
 696 and initial validation results. *Journal of Geophysical Research: Space Physics*,
 697 *107*(A6), SMP–11.
- 698 Anderson, B., Takahashi, K., & Toth, B. (2000). Sensing global Birkeland currents
 699 with Iridium® engineering magnetometer data. *Geophysical Research Letters*,
 700 *27*(24), 4045–4048.
- 701 Baker, D. N., Pulkkinen, T., Angelopoulos, V., Baumjohann, W., & McPherron,
 702 R. (1996). Neutral line model of substorms: Past results and present view.
 703 *Journal of Geophysical Research: Space Physics*, *101*(A6), 12975–13010.
- 704 Boakes, P., Milan, S., Abel, G., Freeman, M., Chisham, G., Hubert, B., & Sotirelis,
 705 T. (2008). On the use of image fuv for estimating the latitude of the
 706 open/closed magnetic field line boundary in the ionosphere. In *Annales geo-*
 707 *physicae* (Vol. 26, pp. 2759–2769).
- 708 Burrell, A., Chisham, G., Milan, S., Kilcommons, L., Chen, Y.-J., Thomas, E., &
 709 Anderson, B. (2020). Ampere polar cap boundaries. In *Annales geophysicae*
 710 (Vol. 38, pp. 481–490).
- 711 Caan, M. N., McPherron, R. L., & Russell, C. T. (1977). Characteristics of the as-
 712 sociation between the interplanetary magnetic field and substorms. *Journal of*
 713 *Geophysical Research*, *82*(29), 4837–4842.
- 714 Clausen, L., Baker, J., Ruohoniemi, J., Milan, S., & Anderson, B. (2012). Dynamics
 715 of the region 1 Birkeland current oval derived from the Active Magnetosphere
 716 and Planetary Electrodynamics Response Experiment (AMPERE). *Journal of*
 717 *Geophysical Research: Space Physics*, *117*(A6).
- 718 Clausen, L., Milan, S., Baker, J., Ruohoniemi, J., Glassmeier, K.-H., Coxon, J., &
 719 Anderson, B. (2013). On the influence of open magnetic flux on substorm
 720 intensity: Ground-and space-based observations. *Journal of Geophysical Re-*
 721 *search: Space Physics*, *118*(6), 2958–2969.
- 722 Cowley, S., & Lockwood, M. (1992). Excitation and decay of solar wind-driven flows
 723 in the magnetosphere-ionosphere system. In *Annales geophysicae* (Vol. 10, pp.
 724 103–115).
- 725 Coxon, J., Milan, S., & Anderson, B. (2018). A review of Birkeland current research
 726 using AMPERE. *Electric currents in geospace and beyond*, 257–278.
- 727 Coxon, J., Milan, S., Clausen, L., Anderson, B., & Korth, H. (2014). A super-
 728 posed epoch analysis of the regions 1 and 2 Birkeland currents observed by
 729 AMPERE during substorms. *Journal of Geophysical Research: Space Physics*,
 730 *119*(12), 9834–9846.
- 731 Davis, T. N., & Sugiura, M. (1966). Auroral electrojet activity index AE and its
 732 universal time variations. *Journal of Geophysical Research*, *71*(3), 785–801.
- 733 DeJong, A. (2014). Steady magnetospheric convection events: How much does
 734 steadiness matter? *Journal of Geophysical Research: Space Physics*, *119*(6),
 735 4389–4399.

- 736 DeJong, A., Ridley, A., & Clauer, C. (2008). Balanced reconnection intervals: Four
737 case studies. *Annales Geophysicae*.
- 738 Dungey, J. W. (1961). Interplanetary magnetic field and the auroral zones. *Physical*
739 *Review Letters*, 6(2), 47.
- 740 Forsyth, C., Rae, I., Coxon, J., Freeman, M., Jackman, C., Gjerloev, J., & Fazaker-
741 ley, A. (2015). A new technique for determining Substorm Onsets and Phases
742 from Indices of the Electrojet (SOPHIE). *Journal of Geophysical Research: Space*
743 *Physics*, 120(12), 10–592.
- 744 Freeman, M., & Morley, S. (2004). A minimal substorm model that explains the ob-
745 served statistical distribution of times between substorms. *Geophysical research*
746 *letters*, 31(12).
- 747 Frey, H., Mende, S., Angelopoulos, V., & Donovan, E. (2004). Substorm onset ob-
748 servations by IMAGE-FUV. *Journal of Geophysical Research: Space Physics*,
749 109(A10).
- 750 Hones Jr., E. (1984). Plasma sheet behavior during substorms. In E. W. H. Jr.
751 (Ed.), *Magnetic Reconnection in Space and Laboratory Plasmas* (Vol. 30, pp.
752 178–184). Washington, D.C.: AGU.
- 753 Hubert, B., Gérard, J.-C., Milan, S. E., & Cowley, S. W. (2017). Magnetic recon-
754 nection during steady magnetospheric convection and other magnetospheric
755 modes. In *Annales geophysicae* (Vol. 35, pp. 505–524).
- 756 Hubert, B., Milan, S., Grocott, A., Blockx, C., Cowley, S., & Gérard, J.-C. (2006).
757 Dayside and nightside reconnection rates inferred from IMAGE FUV and Su-
758 per Dual Auroral Radar Network data. *Journal of Geophysical Research: Space*
759 *Physics*, 111(A3).
- 760 Iijima, T., & Potemra, T. (1976). The amplitude distribution of field-aligned cur-
761 rents at northern high latitudes observed by Triad. *Journal of Geophysical Re-*
762 *search*, 81(13), 2165–2174.
- 763 Iijima, T., & Potemra, T. (1978). Large-scale characteristics of field-aligned currents
764 associated with substorms. *Journal of Geophysical Research: Space Physics*,
765 83(A2), 599–615.
- 766 Iyemori, T. (1990). Storm-time magnetospheric currents inferred from mid-latitude
767 geomagnetic field variations. *Journal of geomagnetism and geoelectricity*,
768 42(11), 1249–1265.
- 769 Kamide, Y., & Kokubun, S. (1996). Two-component auroral electrojet: Impor-
770 tance for substorm studies. *Journal of Geophysical Research: Space Physics*,
771 101(A6), 13027–13046.
- 772 Kan, J., & Lee, L. (1979). Energy coupling function and solar wind-magnetosphere
773 dynamo. *Geophysical Research Letters*, 6(7), 577–580.
- 774 King, J., & Papitashvili, N. (2005). Solar wind spatial scales in and comparisons of
775 hourly Wind and ACE plasma and magnetic field data. *Journal of Geophysical*
776 *Research: Space Physics*, 110(A2).
- 777 Kissinger, J., McPherron, R., Hsu, T.-S., & Angelopoulos, V. (2011). Steady mag-
778 netospheric convection and stream interfaces: Relationship over a solar cycle.
779 *Journal of Geophysical Research: Space Physics*, 116(A5).
- 780 Kissinger, J., McPherron, R., Hsu, T.-S., Angelopoulos, V., & Chu, X. (2012).
781 Necessity of substorm expansions in the initiation of steady magnetospheric
782 convection. *Geophysical research letters*, 39(15).
- 783 Lockwood, M. (1991). On flow reversal boundaries and transpolar voltage in av-
784 erage models of high-latitude convection. *Planetary and space science*, 39(3),
785 397–409.
- 786 Lockwood, M., & Cowley, S. (1992). Ionospheric convection and the substorm cycle.
787 *Proceedings of the International Conference on Substorms (ICS-1)*, 99–109.
- 788 Lockwood, M., Hairston, M., Finch, I., & Rouillard, A. (2009). Transpolar voltage
789 and polar cap flux during the substorm cycle and steady convection events.
790 *Journal of Geophysical Research: Space Physics*, 114(A1).

- 791 Lyons, L. (1995). A new theory for magnetospheric substorms. *Journal of Geophysical*
792 *Research: Space Physics*, *100*(A10), 19069–19081.
- 793 McPherron, R. L. (1970). Growth phase of magnetospheric substorms. *Journal of*
794 *Geophysical Research*, *75*(28), 5592–5599.
- 795 McPherron, R. L., Russell, C. T., & Aubry, M. P. (1973). Satellite studies of mag-
796 netospheric substorms on August 15, 1968: 9. Phenomenological model for
797 substorms. *Journal of Geophysical Research*, *78*(16), 3131–3149.
- 798 McWilliams, K., Pfeifer, J., & McPherron, R. (2008). Steady magnetospheric
799 convection selection criteria: Implications of global superdarn convection mea-
800 surements. *Geophysical research letters*, *35*(9).
- 801 Milan, S. (2004). Dayside and nightside contributions to the cross polar cap poten-
802 tial: placing an upper limit on a viscous-like interaction. *Annales Geophysicae*,
803 *22*, 3771–3777.
- 804 Milan, S. (2009). Both solar wind-magnetosphere coupling and ring current intensity
805 control of the size of the auroral oval. *Geophysical Research Letters*, *36*(18).
- 806 Milan, S. (2013). Modeling birkeland currents in the expanding/contracting polar
807 cap paradigm. *Journal of Geophysical Research: Space Physics*, *118*(9), 5532–
808 5542.
- 809 Milan, S. (2015). Sun et lumière: Solar wind-magnetosphere coupling as deduced
810 from ionospheric flows and polar auroras. In *Magnetospheric Plasma Physics:*
811 *The Impact of Jim Dungey’s Research* (pp. 33–64). Springer.
- 812 Milan, S. (2019). *AMPERE R1/R2 FAC radii. figshare. Dataset.* [https://doi](https://doi.org/10.25392/leicester.data.11294861.v1)
813 [.org/10.25392/leicester.data.11294861.v1](https://doi.org/10.25392/leicester.data.11294861.v1). doi: 10.25392/leicester.data
814 [.11294861.v1](https://doi.org/10.25392/leicester.data.11294861.v1)
- 815 Milan, S. (2020). *Magnetospheric Geonome Project 2010. University of Leicester.*
816 *Dataset.* <https://doi.org/10.25392/leicester.data.12571307.v1>. doi: 10
817 [.25392/leicester.data.12571307.v1](https://doi.org/10.25392/leicester.data.12571307.v1)
- 818 Milan, S., Boakes, P., & Hubert, B. (2008). Response of the expanding/contracting
819 polar cap to weak and strong solar wind driving: Implications for substorm
820 onset. *Journal of Geophysical Research: Space Physics*, *113*(A9).
- 821 Milan, S., Carter, J., Korth, H., & Anderson, B. (2015). Principal component
822 analysis of birkeland currents determined by the active magnetosphere and
823 planetary electrodynamics response experiment. *Journal of Geophysical Re-*
824 *search: Space Physics*, *120*(12), 10–415.
- 825 Milan, S., Clausen, L., Coxon, J., Carter, J., Walach, M.-T., Laundal, K., ... others
826 (2017). Overview of solar wind–magnetosphere–ionosphere–atmosphere cou-
827 pling and the generation of magnetospheric currents. *Space Science Reviews*,
828 *206*(1-4), 547–573.
- 829 Milan, S., Gosling, J., & Hubert, B. (2012). Relationship between interplanetary pa-
830 rameters and the magnetopause reconnection rate quantified from observations
831 of the expanding polar cap. *Journal of Geophysical Research: Space Physics*,
832 *117*(A3).
- 833 Milan, S., Grocott, A., Forsyth, C., Imber, S., Boakes, P. D., & Hubert, B. (2009).
834 A superposed epoch analysis of auroral evolution during substorm growth,
835 onset and recovery: Open magnetic flux control of substorm intensity. *Annales*
836 *Geophysicae*, *27*(2), 659–668.
- 837 Milan, S., Hutchinson, J., Boakes, P., & Hubert, B. (2009). Influences on the radius
838 of the auroral oval. *Annales Geophysicae*, *27*(7), 2913–2924.
- 839 Milan, S., Lester, M., Cowley, S., Oksavik, K., Brittnacher, M., Greenwald, R., ...
840 Villain, J.-P. (2003). Variations in the polar cap area during two substorm
841 cycles. *Annales Geophysicae*, *21*(5), 1121–1140.
- 842 Milan, S., Provan, G., & Hubert, B. (2007). Magnetic flux transport in the Dungey
843 cycle: A survey of dayside and nightside reconnection rates. *Journal of Geo-*
844 *physical Research: Space Physics*, *112*(A1).
- 845 Milan, S., Walach, M.-T., Carter, J., Sangha, H., & Anderson, B. (2019). Sub-

- 846 storm onset latitude and the steadiness of magnetospheric convection. *Journal*
847 *of Geophysical Research: Space Physics*, 124(3), 1738–1752.
- 848 Milan, S., Wild, J., Hubert, B., Carr, C. M., Lucek, E., Bosqued, J., . . . Slavin, J.
849 (2006). Flux closure during a substorm observed by Cluster, Double Star,
850 IMAGE FUV, SuperDARN, and Greenland magnetometers. In *Annales geo-*
851 *physicae* (Vol. 24, pp. 751–767).
- 852 Mooney, M., Forsyth, C., Rae, I., Chisham, G., Coxon, J., Marsh, M., . . . Hubert,
853 B. (2020). Examining local time variations in the gains and losses of open
854 magnetic flux during substorms. *Journal of Geophysical Research: Space*
855 *Physics*.
- 856 Newell, P., & Gjerloev, J. (2011). Evaluation of SuperMAG auroral electrojet indices
857 as indicators of substorms and auroral power. *Journal of Geophysical Research:*
858 *Space Physics*, 116(A12).
- 859 Rostoker, G., Akasofu, S.-I., Foster, J., Greenwald, R., Kamide, Y., Kawasaki, K.,
860 . . . Russell, C. (1980). Magnetospheric substorms—definition and signatures.
861 *Journal of Geophysical Research: Space Physics*, 85(A4), 1663–1668.
- 862 Russell, C. (2000). How northward turnings of the IMF can lead to substorm expan-
863 sion onsets. *Geophysical research letters*, 27(20), 3257–3259.
- 864 Sergeev, V., Kubyshkina, M., Liou, K., Newell, P., Parks, G., Nakamura, R., &
865 Mukai, T. (2001). Substorm and convection bay compared: Auroral and mag-
866 netotail dynamics during convection bay. *Journal of Geophysical Research:*
867 *Space Physics*, 106(A9), 18843–18855.
- 868 Sergeev, V., Pellinen, R. J., & Pulkkinen, T. (1996). Steady magnetospheric convec-
869 tion: A review of recent results. *Space Science Reviews*, 75(3-4), 551–604.
- 870 Siscoe, G., & Huang, T. (1985). Polar cap inflation and deflation. *Journal of Geo-*
871 *physical Research: Space Physics*, 90(A1), 543–547.
- 872 Slavin, J., Fairfield, D., Lepping, R., Hesse, M., Ieda, A., Tanskanen, E., . . . others
873 (2002). Simultaneous observations of earthward flow bursts and plasmoid ejec-
874 tion during magnetospheric substorms. *Journal of Geophysical Research: Space*
875 *Physics*, 107(A7), SMP–13.
- 876 Troshichev, O., Dmitrieva, N., & Kuznetsov, B. (1979). Polar cap magnetic activity
877 as a signature of substorm development. *Planetary and space science*, 27(3),
878 217–221.
- 879 Troshichev, O., Janzhura, A., & Stauning, P. (2006). Unified PCN and PCS indices:
880 Method of calculation, physical sense, and dependence on the IMF azimuthal
881 and northward components. *Journal of Geophysical Research: Space Physics*,
882 111(A5).
- 883 Walach, M.-T., & Milan, S. (2015). Are steady magnetospheric convection events
884 prolonged substorms? *Journal of Geophysical Research: Space Physics*, 120(3),
885 1751–1758.
- 886 Waters, C., Anderson, B., & Liou, K. (2001). Estimation of global field aligned
887 currents using the Iridium® system magnetometer data. *Geophysical Research*
888 *Letters*, 28(11), 2165–2168.